The Role of Ice Nuclei Recycling in the Maintenance of Cloud Ice in Arctic Mixed-Phase Stratocumulus

Amy Solomon[12], Graham Feingold[2], and Matthew D. Shupe[12]

(1) Cooperative Institute for Research in Environmental Sciences, University of Colorado Boulder, Boulder, Colorado, USA.

(2) Earth System Research Laboratory, National Oceanic and Atmospheric Administration, Boulder, Colorado, USA.

Corresponding author: Amy Solomon, NOAA/ESRL, PSD3, 325 Broadway, Boulder, Colorado 80305-3337, USA. (amy.solomon@noaa.gov)

September 14, 2015

Abstract

This study investigates the maintenance of cloud ice production in Arctic mixed phase stratocumulus in large eddy simulations that include a prognostic ice nuclei (IN) formulation and a diurnal cycle. Balances derived from a mixed-layer model and phase analyses are used to provide insight into buffering mechanisms that maintain ice in these cloud systems. We find that for the case under investigation, IN recycling through subcloud sublimation considerably prolongs ice production over a multi-day integration. This effective source of IN to the cloud dominates over mixing sources from above or below the cloud-driven mixed layer. Competing feedbacks between dynamical mixing and recycling are found to slow the rate of ice lost from the mixed layer when a diurnal cycle is simulated. The results of this study have important implications for maintaining phase partitioning of cloud ice and liquid that determine the radiative forcing of Arctic mixed-phase clouds.

1 Introduction

Reliable climate projections require realistic simulations of Arctic cloud feedbacks. Of particular importance is accurately simulating Arctic mixed-phase stratocumuli (AMPS), which are ubiquitous and play an important role in regional climate due to their impact on the surface energy budget and atmospheric boundary layer structure through cloud-driven turbulence, radiative forcing, and precipitation (Curry et al., 1992; Walsh and Chapman, 1998; Intrieri et al., 2002; Shupe and Intrieri, 2004; Sedlar et al., 2011; Persson, 2012). For example, Bennartz et al. (2012) showed that the extreme melt events observed at Summit, Greenland in July 2012 would not have occurred without the surface radiative forcing produced by AMPS.

AMPS are characterized by a liquid cloud layer with ice crystals that precipitate from cloud base even at temperatures well below freezing (Hobbs and Rangno, 1998; Intrieri et al., 2002; McFarquhar et al., 2007). Radiative cooling near cloud top generates turbulence that maintains the liquid layer and forms an approximately well-mixed layer that extends as far as 500 meters below cloud base. These cloud-driven mixed layers are frequently decoupled from the surface layer, limiting the impact of fluxes of heat, moisture, and aerosols on the cloud layer from below (Solomon et al., 2011; Shupe et al., 2013). However, unlike subtropical cloud-topped boundary layers where decoupling enhances cloud breakup by cutting the cloud system off from the surface source of moisture, decoupled AMPS can persist for extended periods of time due to weak precipitation fluxes out of the mixed layer and relatively moist air entrained into the cloud layer at cloud top (Tjernström et al., 2004; Solomon et al., 2011; Sedlar et al., 2012; Solomon et al., 2014).

AMPS are challenging to model due to uncertainties in ice microphysical processes that determine phase partitioning between ice and radiatively important cloud liquid water (Sandvik et al., 2007; Tjernström et al., 2008; Klein et al., 2009, Karlsson and Svensson, 2011; Barton et al., 2012; Birch et al., 2012; de Boer et al., 2012), which drives turbulence that maintains the system. Phase partitioning depends upon the number, shape, and size of ice crystals, since these determine the efficiency of water vapor uptake by ice and hence the availability of water vapor for droplet formation (Chen and Lamb, 1994; Sheridan et al., 2009; Ervens et al., 2011; Hoose and Möhler, 2012).

Since temperatures in AMPS are too warm for homogenous ice nucleation, ice must form through heterogeneous nucleation. Aerosols with properties to serve as seeds for heterogeneous ice crystal formation are referred to as ice nuclei (IN). A number of different aerosols such as mineral dust (Broadley et al., 2012; Kulkarni et al., 2012; Lüönd et al., 2010; Möhler et al. 2006; Pinti et al., 2012; Welti et al., 2009), soot (DeMott, 1990), sea salts (Wise et al., 2012), and bacteria (Kanji et al., 2011; Levin and Yankofsky, 1983) have been observed to act as IN, all of which nucleate at different temperatures and supersaturation ranges. In addition, observations indicate that nucleation properties are modified by aging and coating of aerosols (Möhler et al., 2005; Cziczo et al. 2009). Heterogeneous ice nucleation can occur by a number of modes: either in the presence of super-cooled droplets, when an aerosol comes into contact with a droplet (contact freezing), is immersed in a droplet (immersion freezing), or by vapor deposition on IN (deposition freezing) (Pruppacher and Klett, 1997).

IN can be entrained into the cloud-driven mixed layer through turbulent mixing from above and/or below. Recent studies indicate that entrainment alone cannot account for observed ice crystal number concentration (N_{ICE}) (Fridlind et al., 2012), motivating the use of diagnostic formulations for ice formation to produce model simulations of AMPS with realistic phase partitioning (Ovchinnikov et al., 2011). While this modeling strategy constrains N_{ICE} to be close to the measured values it eliminates the dynamical-microphysical feedbacks that regulate ice/liquid phase partitioning (Avramov et al., 2011).

Here we investigate a relatively unexplored source of ice production--recycling of ice nuclei in regions of ice subsaturation. AMPS frequently have ice-subsaturated air near the cloud-driven mixed-layer base where falling ice crystals can sublimate, leaving behind IN. This feedback loop is referred to hereon as "recycling". Recycling was found to be significant in large eddy simulations of a single-layer stratocumulus observed during the Department of Energy Atmospheric Radiation Measurement Program's Mixed-Phase Arctic Cloud Experiment (M-PACE; Verlinde et al., 2007; Fan et al., 2009). AMPS observed during M-PACE formed due to a cold-air outbreak, where large fluxes of heat and moisture over the open ocean forced turbulent roll clouds that were coupled to the surface layer. This coupling with the surface layer prevented the identification of the role of dynamics internal to the cloud-driven mixed layer in maintaining phase-partitioning.

In this study we focus on the internal microphysics and dynamics of the cloud-driven mixed layer by investigating processes in an AMPS decoupled from surface sources of moisture, heat, and ice nuclei. We posit that recycling plays a significant role more generally since, for example, assuming an adiabatic vertical profile, a 650 meter-deep mixed layer with a cloud-

top temperature of -16°C requires a water vapor mixing ratio of at least 1.7 g kg^{-1} at mixed-layer base to be saturated with respect to ice, i.e., in order for recycling to be a *negligible* source of ice nuclei in the mixed layer. This value is typically only seen in the Arctic between May-September (Serreze et al., 2012), while persistent AMPS frequently occur outside of these months (Shupe et al., 2011).

We examine the role of IN recycling in maintaining ice production using large eddy simulations of a springtime decoupled AMPS. Three simulations are analyzed; a "Control" with recycling turned on and shortwave radiation turned off (to compare with previous simulations of this case that use different IN formulations and shortwave radiation turned off), "NoRecycle" with IN recycling turned off to identify the impact of recycling on the cloud life-time and phase partitioning, and "SW" with recycling and shortwave radiation turned on to identify the impact of realistic diurnal heating and cooling tendencies on the recycling process. This study builds on previous studies of this case, all of which exclude shortwave radiation (Avramov et al., 2011; Solomon et al., 2011, 2014), by including a prognostic equation for IN and a diurnal cycle. Within this modeling framework we investigate the relative roles of recycling and entrainment of IN in maintaining cloud ice production.

2 Case Description

The case derives from observations of a persistent single-layer Arctic mixed-phase stratocumulus cloud observed near Barrow, AK on 8 April 2008 during the Indirect and Semi-Direct Aerosol Campaign (McFarquhar et al., 2011) (see Fig. 1). The adjacent Beaufort Sea was generally ice covered during this time, with significant areas of open water observed east of Barrow. A 4-K temperature inversion with inversion base at 1.05 km was observed

111 via a radiosonde at 17:34UTC; static stability was near neutral within the mixed layer
112 overlaying a stable near-surface layer with static stability greater than 2 K km^{-1} below 500 m.
113 The water vapor mixing ratio, q_v, decreased from 1.7 g kg^{-1} at the surface to 1.2 g kg^{-1} at
114 cloud top, above which a secondary maximum of 1.6 g kg^{-1} was observed. Winds were east-
115 southeasterly throughout the lowest 2 km.

116 Measurements from ground-based, vertically pointing, 35-GHz cloud radar, micropulse lidar,
117 and dual-channel microwave radiometer at Barrow indicated a mixed-phase cloud layer
118 starting at 8 UTC on 8 April 2008 with a cloud top at approximately 1.5km that slowly
119 descended to approximately 0.5 km over a 26 hour period. At the time of the 17:34 sounding
120 the cloud layer extended into the inversion by 100 m, had a cloud base at 0.9 km, and cloud
121 top at 1.15 km. Cloud ice water path (IWP), derived from cloud radar reflectivity
122 measurements, varied from 20–120 g m^{-2} within 10 min of the sounding, with an uncertainty
123 of up to a factor of 2 (Shupe et al., 2006). Concurrently liquid water path (LWP), derived
124 from dual-channel microwave radiometer measurements, was 39–62 g m^{-2}, with an
125 uncertainty of 20–30 g m^{-2} (Turner et al., 2007).

126 Research flights were conducted by the National Research Council of Canada Convair-580 at
127 22:27-23:00 UTC on 8 April 2008 over the ocean northwest of Barrow (McFarquhar et al.,
128 2011). Droplet concentrations measured by a Particle Measuring Systems Forward Scattering
129 Spectrometer Probe varied between 100 and 200 cm^{-3}. Ice crystal number concentrations
130 measured by Stratton Park Engineering Company 2D-S and Particle Measuring Systems 2D-
131 P optical array probes for sizes larger than 100 mm together averaged 0.4 L^{-1}. IN
132 concentrations measured with the Texas A&M Continuous Flow Diffusion Chamber varied

133 from 0.1 L^{-1} to above 20 L^{-1}. Ice crystal habit estimated using the automated habit
134 classification procedure of Korolev and Sussman (2000) indicated primarily dendritic crystal
135 habits.

136 **3 Model Description**

137 We use the large eddy simulation mode of the Advanced Research WRF model (WRFLES)
138 Version 3.3.1 (Yamaguchi and Feingold, 2012) with the National Center for Atmospheric
139 Research Community Atmospheric Model longwave radiation package (Collins et al., 2004),
140 RRTMG shortwave package (Iacono et al., 2008), the Morrison two-moment microphysical
141 scheme (Morrison et al., 2009), and a 1.5-order turbulent kinetic energy prediction scheme
142 (Skamarock et al., 2008). Surface fluxes are calculated uses the modified MM5 similarity
143 scheme which calculates surface exchange coefficients for heat, moisture, and momentum
144 following Webb (1970) and uses Monin-Obukhov with Carlson-Boland viscous sub-layer
145 and standard similarity functions following Paulson (1970) and Dyer and Hicks (1970).

146 All model runs are initialized with winds, temperature, and water vapor from the 17Z 8 April
147 2008 sounding at Barrow, AK (see Fig.1). Initial surface pressure is 1020 hPa. Divergence is
148 assumed to be $2.5x10^{-6}$ s^{-1} below the temperature inversion and zero above, giving a linear
149 increase in large-scale subsidence from zero at the surface to 2.7 mm s^{-1} at the base of the
150 initial inversion (z=1.1 km). This value for divergence was chosen so that the height of the
151 temperature inversion at cloud top is steady. The divergence used in this study is smaller than
152 the divergence used in the WRFLES study of the same case by Solomon et al. (2014) due to

153 the reduced LWPs in this current study and therefore reduced turbulent entrainment that
154 balances large-scale subsidence in a steady simulation.

155 All simulations are run on a domain of 3.2 × 3.2 × 1.8 km with a horizontal grid spacing of
156 50 m and vertical spacing of 10 m. The domain has 65(x)×65(y)×180(z) gridpoints and is
157 periodic in both the x- and y-directions. The top of the domain is at 1.8 km, which is 0.7 km
158 above cloud top in this case. The model time step is 0.75 s. The structure of the cloud layer is
159 insensitive to changes in resolution and domain size. For example, tests run for Solomon et al.
160 (2014) demonstrated that increasing the vertical and horizontal resolutions by a factor of two
161 resulted in an increase in LWP and IWP by 5% and 1%, respectively, while increasing the
162 domain size by a factor of two in both the x- and y-directions results in an increase in LWP
163 and IWP of less than 1%.

164 Cloud droplets are activated using resolved and subgrid vertical motion (Morrison and Pinto
165 2005) and a log-normal aerosol size distribution (assumed to be ammonium bisulfate and
166 30% insoluble by volume) to derive cloud condensation nuclei spectra following Abdul-
167 Razzak and Ghan (2000). The aerosol accumulation mode is specified with concentrations of
168 165 cm^{-3}, modal diameter of 0.2 μm, and geometric standard deviation of 1.4 mm, based on
169 in situ ISDAC measurements. In this formulation, IN and cloud condensation nuclei are
170 treated as separate species.

171 Temperature and moisture profiles are nudged to the initial profiles in the top 400 m of the
172 domain with a time scale of 1 hour. The model is initialized with winds, temperature, and
173 water vapor similar to the Control integration from Solomon et al. (2014). Horizontal winds
174 are nudged to the initial profiles at and above the initial inversion base with a timescale of 2

hours. Initial temperature and subgrid turbulent kinetic energy (TKE) are perturbed below the top of the mixed layer with pseudo-random fluctuations with amplitudes of +/- 0.1 K and 0.1 $m^2\ s^{-2}$, respectively. The liquid layer is allowed to form in the absence of ice during the first hour of the integration to prevent potential glaciation during spinup.

The cloud-driven mixed layer is defined as the region where the liquid-ice water static energy is approximately constant with height. We define the boundaries of the mixed-layer top and base to occur where the slopes of liquid-ice static energy exceed $7x10^{-3}$ K m^{-1} and $1x10^{-3}$ K m^{-1}, respectively. Cloud top and base are defined as the heights where cloud water mixing ratio, q_c, is equal to $1x10^{-4}$ g kg^{-1}.

Nested Weather Research and Forecasting (WRF) model simulations of this case performed with an inner grid at LES resolution (Solomon et al. 2011) demonstrate that moisture is provided to the cloud system by a total water inversion at cloud top and that the mixed layer does not extend to the surface, i.e., the mixed layer is largely decoupled from surface sources of moisture. In addition, the nested simulations indicate that cloud liquid water, q_c, is maintained within the temperature inversion by downgradient turbulent fluxes of q_v from above and direct condensation driven by radiative cooling. These processes cause at least 20% of q_c to extend into the temperature inversion.

WRFLES has been modified to include a prognostic equation for IN number concentration (N_{IN}),

$$\frac{\partial N_{IN}}{\partial t} + ADV + DIFF = \left.\frac{\delta N_{IN}}{\delta t}\right|_{activation} + \left.\frac{\delta N_{IN}}{\delta t}\right|_{sublimation} \quad (1)$$

where ADV represents advection and DIFF represents turbulent diffusion. Activation is also referred to as nucleation of ice and sublimation is also referred to as recycling of IN.

Here we adopt an empirical approach by initializing N_{IN} with an observationally based relationship expressing the number of available IN as a function of temperature in regions of water-saturation (DeMott et al., 2010),

$$N_{IN} = \mathrm{F} * 0.117 \exp\left(-0.125 * (\mathrm{T} - 273.2)\right) \quad (2)$$

where F is an empirically derived scale factor and T is temperature in Kelvin. Sixteen prognostic equations are integrated for N_{IN} in equally spaced temperature intervals with nucleation thresholds between -20.2°C and -15.5°C (see Fig. 2). Therefore, additional IN become available for activation with decreasing temperature and as the cloud layer cools. IN number concentrations are initially specified using equation 2, such that the initial IN in bin *k* is equal to the number of IN calculated by equation 2 at the threshold temperature *k + 1* minus that calculated at temperature *k*. After the initial time 50% of the IN available in a bin nucleates if the in-situ temperature is below the threshold temperature and the local conditions exceed water saturation. Therefore, initial N_{IN} concentrations are a function of the nucleation threshold temperatures and are independent of the in-situ temperature. The in-situ temperature in regions of water saturation determines how many IN are activated. The activation of 50% of the available IN is used to take deviations from the empirical derivation into account, however results are insensitive to this parameter (not shown). Due to the pristine dendritic nature of the observed crystals, ice shattering and aggregation are neglected in the simulations and sublimation returns one N_{IN} per crystal.

214 N_{IN} (in units of L^{-1}) integrated over the domain in each temperature bin k at time t is equal to

$$\overline{N}_{IN}(k,t) = \iiint N_{IN}(x,y,z,k,t)\ dx\ dy\ dz. \quad (3)$$

215 Upon sublimation, the modification of activation thresholds that can occur for previously
216 nucleated IN, i.e. preactivation (Roberts and Hallett, 1967), is not considered and N_{IN} are
217 returned to each bin k with weighting

$$W_k = [\overline{N}_{IN}(k,0) - \overline{N}_{IN}(k,t)\ ]/\ \overline{N}_{IN}(k,0) \quad (4)$$

218 where W_k is normalized such that $\sum W_k = 1$. The W_k are recalculated each time step. In this
219 way, IN are recycled preferentially to each of the 16 temperature bins from which they
220 originated (Feingold et al., 1996).

221 The factor F in Eq. (2) is set to 4 for all simulations yielding an initial N_{IN} summed over all
222 bins at every gridpoint equal to 5.8 L^{-1} at 20.2°C, compared to 10 L^{-1} used in LES studies of
223 the same case presented in Avramov et al. (2011). Using a discrete bin formulation to
224 represent eq. (2) and assigning the coldest bin to the coldest temperature reached by the
225 Control simulation (-20.2°C) results in 3.26 L^{-1} in the warmest bin and 0.23 L^{-1} additional IN
226 that are available for nucleation in the coldest bin. Given the initial temperatures in the cloud
227 layer, all IN from the first bin in the cloud layer nucleate. This causes an initial spike in cloud
228 ice number concentration, which also causes a large precipitation flux out of the mixed layer.
229 It takes approximately 6 hours for the cloud layer to reach a quasi-equilibrium with steady
230 cloud ice production. Supplementary integrations were done to test for robustness of the
231 results presented in Section 4 by varying initial IN concentrations, i.e., the factor F, (shown

232 in Fig. 3) and by varying snow density and fall speeds (shown in Fig. 4). Fig. 3 shows that
233 the simulation maintains ice production when the initial N_{IN} is increased or decreased by ~3
234 L^{-1} relative to Control. Fig. 4 shows that the simulations maintain quasi-steady ice and liquid
235 water paths after an initial spinup but the amount of ice produced is sensitive to the snow fall
236 speed.

237 Crystal size distributions for averaged values of ice water mixing ratio and number
238 concentration from the Control integration are shown in Fig. 5. These crystal size
239 distributions are consistent with the Avramov et al. (2011) simulations of this case where
240 crystal habits are assumed to be high-density pristine dendrites. The distribution shown in Fig.
241 5 underestimates the number of large (greater than 5mm) crystals as estimated by the 2D-S
242 and 2D-P probes (see Avramov et al. (2011) for a detailed discussion of the measurements).

243 The Control integration is run with shortwave radiation turned off in order to compare with
244 previous LES studies of this case (Avramov et al. 2011; Solomon et al. 2014). The results of
245 Control are compared to two additional simulations; one with IN recycling turned off
246 (hereafter "NoRecycle") and one with recycling and shortwave radiation both turned on
247 (hereafter "SW"). SW is used to investigate how the diurnal cycle impacts IN recycling and
248 ice formation. All runs use the same setup except SW has subsidence reduced by 30% to
249 keep the mixed-layer top from lowering appreciably because of smaller LWPs. This allows
250 for direct comparisons of mixed layer structure and fluxes at the mixed layer boundaries. The
251 NoRecycle run is started from the Control run at hour 6 to prevent the two simulations from
252 diverging due to spinup. The first six hours of integration are not used in the analysis to allow
253 for the spinup of cloud ice. Hours 6-40 are used for analysis of the Control and NoRecycle

simulations and hours 16-76 are used for analysis of the SW simulation to allow for multiple diurnal cycles.

4 Model Results

4.1 Control Integration

In the quasi-steady Control integration, the mixed-layer depth is approximately 850 m and comprises a 375 m deep mixed-phase cloud layer (henceforth "the cloud layer"), extending above the mixed-layer top by 25 m, and a 500 m subcloud layer below (Fig. 6). IN are produced by sublimation of ice crystals below the cloud layer, advected to the cloud layer by turbulence, and activated as ice crystals (Fig. 6). Ice that forms in the cloud layer is transported vertically by turbulence, precipitates to cloud base and below, and sublimates below the cloud layer. At the mixed-layer base, an increase in N_{ICE} due to precipitation approximately balances a decrease in N_{ICE} due to sublimation. These processes constitute a feedback through which ice production and IN recycling are closely related. This feedback between ice production and IN in the mixed layer is linked to dynamic-thermodynamic tendencies, which sustain a subsaturated subcloud layer because the decrease in relative humidity due to an upward turbulent vapor flux exceeds the increase due to sublimation.

The time evolution of horizontally-averaged IN advection plus subsidence (Fig. 7a) shows that the majority of IN activate at cloud base, which is a bit warmer than cloud top but is sufficiently cold to activate many of the IN. However, IN from bins with colder threshold temperatures are advected higher into the cloud where they activate at their threshold temperature. A secondary maximum is seen at cloud top where the coldest temperatures are

275 found. Also, it is seen that IN are advected into the cloud layer at cloud top for the first 15-18
276 hours, but this source of IN decreases as IN in the upper entrainment zone are depleted. The
277 turbulent mixing of snow and ice in the mixed-phase cloud layer is clearly seen in Fig. 7b,
278 where ice plus snow number concentrations are well-mixed in the cloud layer. Given the
279 efficient mixing by the turbulent eddies, it is not possible to identify whether ice has
280 nucleated at cloud base or cloud top from the ice number concentrations alone. Fig. 7 also
281 shows the time-height cross sections of horizontally-averaged water vapor mixing ratio and
282 relative humidity with respect to ice. These figures show that the continuous drying and
283 cooling of the mixed layer results in continuous sublimation in the subcloud layer.

284 LWP and IWP remain steady until hour 16 of the simulation, and decrease slowly thereafter
285 (solid lines in Fig. 8a). LWP and IWP magnitudes are within the observational estimates for
286 this case. In addition, the cloud system is sustained over a multi-day period similar to
287 measurements taken during ISDAC. Continuous cloud-top cooling causes the minimum
288 horizontally-averaged temperature (near cloud top) to decrease from -17.5^{o}C to -20^{o}C from
289 hour 10 to hour 40 (Fig. 8b).

290 Over the 40-hour integration, the mixed layer remains decoupled from the surface (Fig. 8c).
291 However, this does not prevent the number concentration of ice crystals (N_{ICE}) in the cloud
292 layer from remaining relatively steady, decreasing from vertically integrated values of 372 to
293 365 m L^{-1} (Fig. 8d, or in terms of vertically averaged cloud layer values, 1.2 L^{-1} to 1.1 L^{-1}).
294 By contrast, while N_{ICE} is maintained in the cloud layer, N_{IN} in the subcloud layer decreases
295 significantly from 2 L^{-1} to 0.2 L^{-1} over the same period. Therefore, even though more N_{ICE}
296 are lost from the cloud than are activated (Fig. 9a), the relatively constant flux of IN into the

297 cloud layer (Fig. 9b) allows N_{ICE} in the cloud to decrease at a slower rate than N_{IN} in the
298 subcloud layer. The continuous loss of N_{IN} in the subcloud layer is due to the IN flux into the
299 cloud layer exceeding the N_{IN} gained through sublimation and turbulent advection at mixed-
300 layer base (Fig. 9b). This loss is not mitigated by entrainment at mixed-layer top, which is
301 found to be negligible (Fig. 9c), consistent with Fridlind et al. (2011).

302 The feedback loops discussed above are illustrated by the conceptual diagram in Fig. 10,
303 where any change to one link in the cycle leads to an increase or decrease in ice production.
304 For example, a decrease in the turbulent advection of N_{IN} into the cloud layer, slows the
305 activation of IN, reduces the precipitation flux into the subcloud layer, reducing sublimation
306 and availability of IN below cloud base. Both dynamics and thermodynamics play a role in
307 the buffering aspect of these feedback loops since, for example, the slowing of IN activation
308 in the example above would lead to increased cloud liquid production, cloud-top radiative
309 cooling, and enhanced turbulent mixing, which would lead to increased transport of IN into
310 the cloud layer and therefore increased activation of IN.

311 ***4.2 Impact of turning off recycling***

312 When IN recycling is turned off, all IN that activate are lost from the system. This results in a
313 more rapid loss of IN, a decrease in IWP, and a rapid increase in LWP (Fig. 8a,d, dashed
314 lines), in contrast to the measurements that show a steady liquid layer and consistent ice
315 production. Increased cloud liquid water when recycling is turned off results in increased
316 radiative cooling at cloud top, which causes the cloud-driven mixed layer to cool more
317 rapidly (Fig. 8b). These results demonstrate the importance of IN recycling in regulating

phase partitioning. The rapid increase in LWP increases cloud-generated turbulence via enhanced radiative cooling and increases the turbulent mixing of IN from the subcloud layer into the cloud layer, contributing to a more rapid depletion of IN relative to the Control integration. This process eventually becomes limited due to depletion of IN in the reservoir below (Fig. 9b). Due to the additional activation of IN as the cloud layer cools, ice production is maintained in the absence of recycling and the activation of IN in the cloud layer exceeds the upward IN flux at cloud base (Fig. 9a,b). However, the diminishing N_{IN} in the subcloud layer limits IN activation and N_{ICE} rapidly decreases in the cloud layer (Fig. 8d).

4.3 Impact of diurnal cycle

A diurnal cycle is added to the Control simulation in order to investigate how the feedback loops identified in the Control and NoRecycle runs are modified with realistic transient heating and cooling tendencies due to variations in incoming shortwave radiation. A question that is addressed in this diurnal simulation is, to what extent is the continuous production of ice in the Control simulation due to the lack of incoming shortwave radiation, which may overestimate the cooling tendencies in the cloud layer, resulting in an overestimate of IN activation? In addition, we investigate whether allowing for a realistic diurnal cycle provides for additional negative or "buffering" feedbacks.

Adding a diurnal cycle to the Control simulation produces a diurnal peak in downwelling surface shortwave radiation of 510 W m^{-2} and 6 hours of total darkness per day (Fig. 11b). As shortwave radiation increases, the net radiative cooling near cloud top diminishes, which decreases cloud-generated turbulence, decreasing LWP and cloud-layer thickness. In addition,

339 it is seen that the peak daily LWP coincides with zero shortwave radiation when in-cloud
340 turbulence and cloud thickness are largest (Fig. 11a). These values are on the low end but
341 within the measurements for this ISDAC case.

342 Fig. 11a,b shows that LWP and IWP variability is predominantly driven by the diurnal cycle.
343 However, IWP variability is seen to lag LWP by 3-4 hours because as shortwave radiation
344 decreases the cloud layer cools, which increases activation of IN, increasing N_{ICE}, allowing
345 more ice crystals to grow, which increases IWP (Fig. 11a,b). Similar to the Control
346 simulation subcloud N_{IN} decreases at a faster rate than cloud layer N_{ICE}, but allowing for the
347 warming and cooling tendencies in the diurnal cycle results in cloud layer N_{ICE} that decreases
348 40% more slowly than in the Control simulation (Fig. 11c).

349 Precipitation and turbulent mixing of N_{ICE} (hereafter turbulent mixing is referred to as
350 "T_{ICE}") at cloud base are out of phase by 10 hours (Fig. 11d), with turbulence leading
351 precipitation. When shortwave radiation is weak or absent, the increase in N_{ICE} eventually
352 becomes limited by a decreasing turbulent mixing of IN ("T_{IN}") into the cloud layer from
353 below, as recycling slows due to a decrease in N_{ICE} flux from the cloud layer (Fig. 11d,f).
354 When shortwave radiation is strong, reduction in IWP is limited by weaker precipitation
355 losses, and attendant weaker sublimation and IN flux into the cloud layer (Fig. 11d,f).
356 Entrainment of N_{IN} at the mixed-layer top is insignificant throughout the integration (Fig.
357 11e).

358 **5 Analysis from a mixed-layer perspective**

The results discussed in Section 4 can be understood from balances in a well-mixed layer with sources/sinks at the upper and lower boundaries. Total particle concentration (N_{IN}+N_{ICE}) is only changed by fluxes at the mixed-layer boundaries when recycling is allowed. These fluxes are entrainment of N_{IN} at mixed-layer top and turbulent mixing of both N_{ICE} and N_{IN} (T_{ICE} and T_{IN}) and precipitation of N_{ICE} (P) at mixed-layer base. Since there are no sources and sinks of N_{IN}+N_{ICE} within the mixed layer, the horizontally-averaged N_{IN}+N_{ICE} flux ($f(z)$) must vary linearly from mixed-layer base to mixed-layer top (Lilly, 1968; Bretherton and Wyant, 1997). If it is assumed that f at the mixed-layer base is downward (assumed negative in this formulation) and f at the mixed-layer top is negligible (robust assumptions for a scenario where ice is precipitating from the mixed layer and entrainment is weak), then

$$f(z) = R * \frac{H - z}{H - B}, \qquad B \leq z \leq H \tag{5}$$

where H is the mixed-layer height, B is the mixed-layer base and R is the total N_{IN}+N_{ICE} flux at the mixed-layer base,

$$R = f|_{\text{Mixed-Layer Base}} = [P + T_{ICE} + T_{IN}]_{\text{Mixed-Layer Base}}, \tag{6}$$

and

$$[T_{ICE} + T_{IN}]_{\text{Cloud Base}} \approx [f - P]_{\text{Cloud Base}}. \tag{7}$$

Since $f < 0$, the turbulent flux of N_{IN} into the cloud layer plus the turbulent flux of N_{ICE} into the subcloud layer is always less than precipitation of N_{ICE} at cloud base. In addition, in a

slowly evolving state where $T_{IN}|_{\text{Mixed-Layer Base}} > 0$, total IN flux due to sublimation in the mixed layer, S, can be written as

$$S \approx [P + T_{ICE}]_{\text{Mixed-Layer Base}} - [P + T_{ICE}]_{\text{Cloud Base}} \quad (8a)$$

$$\approx [f - T_{IN}]_{\text{Mixed-Layer Base}} - [f - T_{IN}]_{\text{Cloud Base}} \quad (8b)$$

and since $f|_{\text{Mixed-Layer Base}}$ is downward and $f|_{\text{Mixed-Layer Top}}$ is negligible (eq. 5),

$$S < T_{IN}|_{\text{Cloud Base}} - T_{IN}|_{\text{Mixed-Layer Base}} \quad (8c)$$

$$< T_{IN}|_{\text{Cloud Base}}. \quad (8d)$$

Thus in a well-mixed layer with an upward $T_{IN}|_{\text{Mixed-Layer Base}}$, sublimation is always less than the flux of N_{IN} into the cloud layer.

Based on results from Control, precipitation of N_{ICE} at cloud base is sufficient to balance the upward turbulent flux of N_{IN} (i.e., $|T_{IN}| \gg |T_{ICE}|$ at cloud base). Therefore, in a well-mixed layer with precipitation of N_{ICE} at the mixed-layer base that is larger in magnitude than an upward turbulent N_{IN} flux at the mixed-layer base, and assuming negligible entrainment at the mixed-layer top

$$|P|_{\text{Cloud Base}} > T_{IN}|_{\text{Cloud Base}} > S. \quad (9)$$

However, if all N_{ICE} sublimate in the mixed layer and the upward turbulent flux of N_{IN} dominates at the mixed-layer base then $f > 0$ and

$$T_{IN}|_{\text{Cloud Base}} > |P|_{\text{Cloud Base}} = S, \quad (10)$$

the mixed layer gains $N_{IN}+N_{ICE}$ over time, resulting in a continuously increasing ice production in the cloud layer. In the presence of shortwave radiation (i.e., in the SW simulation), $T_{IN}|_{\text{Cloud Base}}$ is also greater than $|P|_{\text{Cloud Base}}$ after a period of weakened turbulence and weaker precipitation at the mixed-layer base, due to increased activation of N_{IN} due to decreasing shortwave radiation.

If IN entrainment at the mixed-layer top is not negligible then $f(z)$ must be modified to include fluxes at the mixed-layer top and $|f|_{\text{Cloud Base}}$ will increase. If $|f|_{\text{Cloud Base}}$ increases such that $f_{\text{Cloud Base}} < P_{\text{Mixed-Layer Base}}$, then sublimation will exceed $T_{IN}|_{\text{Cloud Base}}$.

This mixed-layer analysis provides a framework to understand the results presented in Section 4. Specifically, sublimation being less than the turbulent flux of IN is seen to be a property of a well-mixed layer where the total flux at mixed-layer base is downward and the total flux at the mixed-layer top is negligible. In the case where the mixed layer is saturated with respect to ice, sublimation is equal to zero and the turbulent flux of IN at the mixed-layer base is less that the turbulent flux of IN at the cloud base, reducing the flux of IN into the cloud layer. The relationships outlined in this section are appropriate for any AMPS with weak entrainment at cloud top, weak large-scale advective fluxes, and net downward fluxes at the mixed-layer base.

6 Analysis of Buffered Feedbacks in SW

406 Phase diagrams highlight the processes involved in ice production when a diurnal cycle is
407 allowed (following the arrows from green to blue to black to red in Fig. 12a,b). When
408 incoming shortwave radiation is a maximum, recycling (sublimation) is seen to be at a
409 minimum. This is counterintuitive since subcloud relative humidity is low at this time, which
410 would be expected to produce increased sublimation. However, due to weak turbulent mixing
411 between the cloud and subcloud layers the net N_{ICE} flux into the subcloud layer is weak,
412 resulting in weak sublimation and recycling. This situation is reversed as shortwave radiation
413 decreases, since increased cloud-top cooling increases cloud-driven turbulent mixing, which
414 allows recycling to increase in the regions of reduced subcloud relative humidity. As is seen
415 in the conceptual diagram (Fig. 10), this then leads to an increased N_{ICE} flux into the
416 subcloud layer (green arrows, Fig. 12). However, N_{ICE} in the cloud layer doesn't begin to
417 increase until activation in the cloud layer exceeds the flux of N_{ICE} into the subcloud layer
418 (green arrows). This cycle is further amplified as shortwave radiation decreases, namely,
419 decreased shortwave radiation increases cloud-driven turbulence, increasing the flux of IN
420 into the cloud layer, increasing the activation of IN, which increases N_{ICE} in the cloud layer
421 and the N_{ICE} flux from the cloud layer into the subcloud layer (blue arrows).

422 When incoming shortwave radiation is a minimum, more N_{IN} are activated because the cloud
423 layer cools. However, again we see that N_{ICE} tendencies due to thermodynamics are buffered
424 by the slowing of turbulence-driven feedbacks due to a thickening of the cloud layer. Thus, a
425 net increase in N_{ICE} in the cloud layer, commensurate with an increased IWP and
426 precipitation (black arrows), is buffered by a decrease in the downward turbulent mixing of
427 N_{ICE}, which reduces recycling, slowing the feedback loop (see Fig. 10). During the morning
428 hours, as the cloud layer warms and thins and ice activation becomes less efficient,

turbulence continues to decline, slowing the recycling feedback process to the point where limited IN fluxes to the cloud layer inhibit ice production and N_{ICE} declines (red arrows).

7 Summary

We have demonstrated that sustained recycling of IN through a drying subcloud layer and additional activation of N_{IN} due to a cooling cloud layer are sufficient to maintain ice production, and regulate liquid production over multiple days in a decoupled AMPS.

This study provides an idealized framework to understand feedbacks between dynamics and microphysics that maintain phase-partitioning in AMPS. In addition, we have shown that modulation of the cooling of the cloud layer and the humidity of the subcloud layer by the diurnal cycle buffers the mixed-layer system from a loss of particles and promotes the persistence of a mixed-phase cloud system. The results of this study provide insight into the mechanisms and feedbacks that may maintain cloud ice in AMPS even when entrainment of IN at the mixed-layer boundaries is weak. While the balance of these processes changes depending upon the specific conditions of the cloud layer, for example whether the cloud layer is coupled to the surface layer, the mechanisms detailed in this paper will manifest to some degree and therefore the current study provides a framework for understanding the role of recycling in maintaining phase-partitioning in AMPS.

446 **Author Contributions:**

447 A.S., G.F., and M.D.S. conceived and designed the experiments; A.S. performed the
448 simulations; A.S., G.F., and M.D.S. analyzed the model results and co-wrote the paper.

449 **Acknowledgements:**

450 The authors acknowledge discussions with Alex Avramov, Chris Cox, Gijs de Boer, Barbara
451 Ervens, and Ann Fridlind, and Takanobu Yamaguchi for developing the software to run
452 WRF as a large eddy simulation. This research was supported by the Office of Science
453 (BER), U.S. Department of Energy (DE-SC0011918) and the National Science Foundation
454 (ARC-1023366).

455 **References**

456 Abdul-Razzak, H. and Ghan, S. J.: A parameterization of aerosol activation 2. Multiple
457 aerosol types, J. Geophys. Res., 105, 6837–6844, 2000.

458 Avramov, A., Ackerman, A. S., Fridlind, A. M., van Diedenhoven, B., Botta, G., Aydin, K.,
459 Verlinde, J., Korolev, A. V., Strapp, J. W., McFarquhar, G. M., Jackson, R., Brooks, S.
460 D., Glen, A., and Wolde, M.: Toward ice formation closure in Arctic mixed-phase
461 boundary layer clouds during ISDAC, J. Geophys. Res., 116, D00T08,
462 doi:10.1029/2011JD015910, 2011.

463 Barton, N. P., Klein, S. A., Boyle, J. S., and Zhang, Y. Y.: Arctic synoptic regimes:
464 Comparing domain wide Arctic cloud observations with CAM4 and CAM5 during
465 similar dynamics, J. Geophys. Res., 117, D15205, doi:10.1029/2012JD017589, 2012.

466 Bennartz, R., Shupe, M., Turner, D., Walden, V., Steffen, K., Cox, C., Kulie, M. S., Miller,
467 N., and Pettersen, C.: July 2012 Greenland melt extent enhanced by low-level liquid
468 clouds, Nature, 496, 83-86, doi:10.1038/nature12002, 2012.

469 Birch, C. E., Brooks, I. M., Tjernström, M., Shupe, M. D., Mauritsen, T., Sedlar, J., Lock, A.
470 P., Earnshaw, P., Persson, P. O. G., Milton, S. F., and Leck, C.: Modeling atmospheric
471 structure, cloud and their response to CCN in the central Arctic: ASCOS case studies,
472 Atmos. Chem. Phys., 12, 3419-3435, doi:10.5194/acp-12-3419-2012, 2012.

473 Bretherton, C. S. and Wyant, M. C.: Moisture transport, lower-tropospheric stability, and
474 decoupling of cloud-topped boundary layers, J. Atmos. Sci., 54, 148-167, 1997.

475 Broadley, S., Murray, B., Herbert, R., Atkinson, J., Dobbie, S., Malkin, T., Condliffe, E., and
476 Neve, L.: Immersion mode heterogeneous ice nucleation by an illite rich powder
477 representative of atmospheric mineral dust, Atmos. Chem. Phys., 12:287{307,

478 doi:10.5194/acp-12-287-2012, 2012.
479 Chen, J.-P. and Lamb, D.: The theoretical basis for the parameterization of ice crystal habits:
480 Growth by vapor deposition, J. Atmos. Sci., 51, 1206–1222, doi:10.1175/1520-
481 0469(1994)051<1206:TTBFTP>2.0.CO;2, 1994.
482 Collins, W. D., Rasch, P. J., Boville, B. A., Hack, J. J., McCaa, J. R., Williamson, D. L., and
483 Briegleb, B. P.: Description of the NCAR Community Atmosphere Model (CAM 3.0),
484 NCAR Technical Note, NCAR/TN-464+STR, 226 pp., 2004.
485 Curry, J. and Ebert, E. E.: Annual cycle of radiation fluxes over the Arctic Ocean: Sensitivity
486 to cloud optical properties, J. Climate, 5, 1267–1280, 1992.
487 Cziczo, D., Froyd, K., Gallavardin, S., Moehler, O., Benz, S., Saathoff, H., and Murphy, D.:
488 Deactivation of ice nuclei due to atmospherically relevant surface coatings, Environ.
489 Res. Lett., 4:044013, doi:10.1088/1748-9326/4/4/044013, 2009.
490 de Boer, G., Chapman, W., Kay, J. E., Medeiros, B., Shupe, M. D., Vavrus, S., and Walsh, J.:
491 A characterization of the present-day Arctic atmosphere in CCSM4, J. Climate, 25,
492 2676–2695, 2012.
493 DeMott, P. J.: An exploratory study of ice nucleation by soot aerosols, J. Appl. Meteorol.,
494 29(10), 1072–1079, 1990.
495 DeMott, P. J., Prenni, A. J., Liu, X., Petters, M. D., Twohy, C. H., Richardson, M. S.,
496 Eidhammer, T., Kreidenweis, S. M., and Rogers, D. C.: Predicting global atmospheric
497 ice nuclei distributions and their impacts on climate, P. Natl. Acad. Sci. USA, 107,
498 11217-11222, doi:10.1073/pnas.0910818107, 2010.
499 Dyer, A. J. and Hicks, B. B.: Flux-gradient relationships in the constant flux layer, Q. J. Roy.
500 Meteor. Soc., 96, 715–721, 1970.

501 Ervens, B., Feingold, G., Sulia, K., and Harrington, J.: The impact of microphysical
502 parameters, ice nucleation mode, and habit growth on the ice/liquid partitioning in
503 mixed-phase Arctic clouds, J. Geophys. Res., 116, D17205,
504 doi:10.1029/2011JD015729, 2011.
505 Fan, J., Ovchinnikov, M., Comstock, J. M., McFarlane, S. A., and Khain, A.: Ice formation
506 in Arctic mixed-phase clouds: Insights from a 3-D cloud-resolving model with size-
507 resolved aerosol and cloud microphysics, J. Geophys. Res., 114, D04205,
508 doi:10.1029/2008JD010782, 2009.
509 Feingold, G., Kreidenweis, S. M., Stevens, B., and Cotton, W. R.: Numerical simulation of
510 stratocumulus processing of cloud condensation nuclei through collision-coalescence, J.
511 Geophys. Res., 101, 21,391-21,402, 1996.
512 Fridlind, A. M., van Diedenhoven, B., Ackerman, A. S., Avramov, A., Mrowiec, A.,
513 Morrison, H., Zuidema, P., and Shupe, M. D.: A FIRE-ACE/SHEBA case study of
514 mixed-phase Arctic boundary-layer clouds: Entrainment rate limitations on rapid
515 primary ice nucleation processes, J. Atmos. Sci., 69, 365-389, doi:10.1175/JAS-D-11-
516 052.1, 2012.
517 Hobbs, P. V. and Rangno A. L.: Microstructure of low and middle- level clouds over the
518 Beaufort Sea, Q. J. Roy. Meteor. Soc., 124, 2035-2071, 1998.
519 Hoose, C. and Möhler, O.: Heterogeneous ice nucleation on atmospheric aerosols: a review
520 of results from laboratory experiments, Atmos. Chem. Phys., 12, 9817-9854,
521 doi:10.5194/acp-12-9817-2012, 2012.
522 Iacono, M. J., Delamere, J. S., Mlawer, E. J., Shephard, M. W., Clough, S. A., and Collins,
523 W. D.: Radiative forcing by long-lived greenhouse gases: Calculations with the AER

524 Radiative transfer models, J. Geophys. Res., 113, D13103, doi:10.1029/2008JD009944,
525 2008.
526 Intrieri, J. M., Fairall, C. W., Shupe, M. D., Persson, P. O. G., Andreas, E., Guest, P. S., and
527 Moritz, R. E.: An annual cycle of Arctic surface cloud forcing at SHEBA, J. Geophys.
528 Res., 107, 8039, doi:10.1029/2000JC000439, 2002.
529 Kanji, Z., DeMott, P., Möhler, O., and Abbatt, J.: Results from the University of Toronto
530 continuous flow diffusion chamber at ICIS 2007: instrument intercomparison and ice
531 onsets for different aerosol types, Atmos. Chem. Phys., 11:31-41, doi:10.5194/acp-11-
532 31-2011, 2011.
533 Karlsson, J. and Svensson, G.: The simulation of Arctic clouds and their influence on the
534 winter surface temperature in present-day climate in the CMIP3 multi-model dataset,
535 Clim. Dynam., 36, 623–635, 2011.
536 Klein, S. A., McCoy, R., Morrison, H., Ackerman, A., Avramov, A., de Boer, G., Chen, M.,
537 Cole, J., DelGenio, A. D., Falk, M., Foster, M., Fridlind, A., Golaz, J.-C., Hashino, T.,
538 Harrington, J., Hoose, C., Khairoutdinov, M., Larson, V., Liu, X., Luo, Y., McFarquhar,
539 G., Menon, S., Neggers, R., Park, S., von Salzen, K., Schmidt, J. M., Sednev, I.,
540 Shipway, B., Shupe, M., Spangenberg, D., Sud, Y., Turner, D., Veron, D., Walker, G.,
541 Wang, Z., Wolf, A., Xie, S., Xu, K.-M., Yang, G., and Zhang, G.: Intercomparison of
542 model simulations of mixed-phase clouds observed during the ARM Mixed-Phase Arctic
543 Cloud Experiment. I: Single-layer cloud, Q. J. Roy. Meteor. Soc., 135, 979–1002, 2009.
544 Korolev, A.: Limitations of the Wegener–Bergeron–Findeisen mechanism in the evolution of
545 mixed-phase clouds, J. Atmos. Sci., 64, 3372–3375, doi:10.1175/JAS4035.1, 2007.

546 Korolev, A. and Sussman, B.: A technique for habit classification of cloud particles, J. Atmos.
547 Oceanic Technol., 17, 1048–1057, 2000.
548 Kulkarni, G., Fan, J., Comstock, J., Liu, X., and Ovchinnikov, M.: Laboratory measurements
549 and model sensitivity studies of dust deposition ice nucleation, Atmos. Chem. Phys.,
550 12:7295-7308, doi:10.5194/acp-12-7295-2012, 2012.
551 Levin, Z. and Yankofsky, S.: Contact versus immersion freezing of freely suspended droplets
552 by bacterial ice nuclei, J. Appl. Meteorol. Clim., 22, 1964-1966, 1983.
553 Lilly, D. K.: Models of cloud-topped mixed layers under a strong inversion, Q. J. Roy.
554 Meteor. Soc., 94, 292–309, 1968.
555 Lüönd, F., Stetzer, O., Welti, A., and Lohmann, U.: Experimental study on ice nucleation
556 ability of size selected kaolinite particles in the immersion mode, J. Geophys. Res.,
557 115:D14201, doi:10.1029/2009JD012959, 2010.
558 McFarquhar, G. M., Zhang, G., Poellot, M. R., Kok, G. L., McCoy, R., Tooman, T., Fridlind,
559 A., and Heymsfield, A. J.: Ice properties of single-layer stratocumulus during the Mixed-
560 Phase Arctic Cloud Experiment: 1. Observations, J. Geophys. Res., 112, D24201,
561 doi:10.1029/2007JD008633, 2007.
562 McFarquhar, G. M., Ghan, S., Verlinde, J., Korolev, A., Strapp, J. W., Schmid, B.,
563 Tomlinson, J. M., Wolde, M., Brooks, S. D., Cziczo, D., Dubey, M. K., Fan, J., Flynn,
564 C., Gultepe, I., Hubbe, J., Gilles, M. K., Laskin, A., Lawson, P., Leaitch, W. R., Liu, P.,
565 Liu, X., Lubin, D., Mazzoleni, C., Macdonald, A.-M., Moffet, R. C., Morrison, H.,
566 Ovchinnikov, M., Shupe, M. D., Turner, D. D., Xie, S., Zelenyuk, A., Bae, K., Freer, M.,
567 and Glen, A.: Indirect and Semi-Direct Aerosol Campaign (ISDAC): The Impact of

568 Arctic Aerosols on Clouds, B. Am. Meteorol. Soc., 92, 183–201,
569 doi:10.1175/2010BAMS2935.1, 2011.
570 Möhler, O., Bütuner, S., Linke, C., Schnaiter, M., Saathoff, H., Stetzer, O., Wagner, R.,
571 Krämer, M., Mangold, A., Ebert, V., and Schurath, U.: Effect of sulfuric acid coating on
572 heterogeneous ice nucleation by soot aerosol particles, J. Geophys. Res., 110:D11210,
573 doi: 10.1029/2004JD005169, 2005.
574 Möhler, O., Field, P., Connolly, P., Benz, S., Saathoff, H., Schnaiter, M., Wagner, R., Cotton,
575 R., Krämer, M., Mangold, A., and Heymsfield, A.: Efficiency of the deposition mode ice
576 nucleation on mineral dust particles, Atmos. Chem. Phys., 6:3007-3021,
577 doi:10.5194/acp-6-3007-2006, 2006.
578 Morrison, H. and Pinto, J. O.: Mesoscale modeling of springtime Arctic mixed-phase
579 stratiform clouds using a new two-moment bulk microphysics scheme, J. Atmos. Sci., 62,
580 3683-3704, 2005.
581 Morrison, H., Thompson, G., and Tatarskii, V.: Impact of cloud microphysics on the
582 development of trailing stratiform precipitation in a simulated squall line: Comparison of
583 one- and two-moment schemes, Mon. Wea. Rev., 137, 991-1007,
584 doi:10.1175/2008MWR2556.1, 2009.
585 Paulson, C. A.: The mathematical representation of wind speed and temperature profiles in
586 the unstable atmospheric surface layer, J. Appl. Meteor., 9, 857–861, 1970.
587 Persson, P. O. G.: Onset and end of the summer melt season over sea ice: Thermal structure
588 and surface energy perspective from SHEBA, Clim. Dynam., 39, 1349-1371,
589 doi:10.1007/s00382-011-1196-9, 2012.

590 Pinti, V., Marcolli, C., Zobrist, B., Hoyle, C., and Peter, T.: Ice nucleation efficiency of clay
591 minerals in the immersion mode, Atmos. Chem. Phys., 12:5859-5878, doi:10.5194/acp-
592 12-5859-2012, 2012.
593 Pruppacher, H. and Klett, J.: Microphysics of clouds and precipitation. Kluwer Academic
594 Publishers, 2nd edition, 1997.
595 Roberts, P. and Hallett, J.: A laboratory study of the ice nucleating properties of some
596 mineral particulates, Q. J. R. Meteorol. Soc., 94, 25 – 34, 1967.
597 Sandvik, A., Biryulina, M., Kvamsto, N., Stamnes, J., and Stamnes, K.: Observed and
598 simulated microphysical composition of Arctic clouds: Data properties and model
599 validation, J. Geophys. Res. 112, D05205, 2007.
600 Sedlar, J., Shupe, M. D., and Tjernström, M.: On the relationship between thermodynamic
601 structure, cloud top, and climate significance in the Arctic, J. Climate, 25, 2374–2393,
602 2012.
603 Sedlar, J., Tjernström, M., Mauritsen, T., Shupe, M. D., Brooks, I. M., Persson, P. O. G.,
604 Birch, C. E., and C. Leck, C.: A transitioning Arctic surface energy budget: The impacts
605 of solar zenith angle, surface albedo and cloud radiative forcing, Clim. Dynam., 37,
606 1643–1660, doi:10.1007/s00382-010-0937-5, 2011.
607 Serreze, M. C., Barrett, A. P., and Stroeve, J.: Recent changes in tropospheric water vapor
608 over the Arctic as assessed from radiosondes and atmospheric reanalyses. J. Geophys.
609 Res., 117, D10104, doi:10.1029/2011JD017421, 2012.
610 Sheridan, L. M., Harrington, J. Y., Lamb, D., and Sulia, K.: Influence of ice crystal aspect
611 ratio on the evolution of ice size spectra during vapor depositional growth, J. Atmos. Sci.,
612 66, 3732–3743, doi:10.1175/2009JAS3113.1, 2009.

613 Shupe, M. D.: A ground-based multiple remote-sensor cloud phase classifier, Geophys. Res.
614 Lett., 34, L2209, doi:10.1029/2007GL031008, 2007.
615 Shupe, M. D and J. M. Intrieri: Cloud radiative forcing of the Arctic surface: The influence
616 of cloud properties, surface albedo, and solar zenith angle, J. Climate, 17, 616-628, 2004.
617 Shupe, M. D, Matrosov, S. Y., and Uttal, T.: Arctic mixed phase cloud properties derived
618 from surface-based sensors at SHEBA, J. Atmos. Sci., 63, 697-811, 2006.
619 Shupe, M. D, Persson, P. O. G., Brooks, I. M., Tjernström, M., Sedlar, J., Mauritsen, T.,
620 Sjogren, S., and Leck, C.: Cloud and boundary layer interactions over the Arctic sea-ice
621 in late summer, Atmos. Chem. Phys., 13, 9379-9400, 2013.
622 Skamarock, W. C., Klemp, J. B., Dudhia, J., Gill, D. O., Barker, D. M., Duda, M. G., Huang,
623 X.-Y., Wang, W., and Powers, J. G.: A description of the Advanced Research WRF
624 version 3, NCAR Tech. Note NCAR/TN-475+STR, 113 pp., 2008.
625 Solomon, A., Morrison, H., Persson, P. O. G., Shupe, M. D., and Bao, J.-W.: Investigation of
626 microphysical parameterizations of snow and ice in Arctic clouds during M-PACE
627 through model-observation comparisons, Mon. Wea. Rev., 137, 3110-3128,
628 doi:10.1175/2009MWR2688.1, 2009.
629 Solomon, A., Shupe, M. D., Persson, P. O. G., and Morrison, H.: Moisture and dynamical
630 interactions maintaining decoupled Arctic mixed-phase stratocumulus in the presence of
631 a humidity inversion, Atmos. Chem. Phys, 11, 10127-10148, doi:10.5194/acp-11-10127-
632 2011, 2011.
633 Solomon, A., Shupe, M. D., Persson, P. O. G., Morrison, H., Yamaguchi, T., Caldwell, P. M.,
634 and de Boer, G.: The sensitivity of springtime Arctic mixed-phase stratocumulus clouds

635 to surface layer and cloud-top inversion layer moisture sources, J. Atmos. Sci., 71, 574-
636 595, doi:10.1175/JAS-D-13-0179.1, 2014.
637 Tjernström, M., Sedlar, J., and Shupe, M. D.: How well do regional climate models
638 reproduce radiation and clouds in the Arctic? An evaluation of ARCMIP simulations, J.
639 Appl. Met. Clim., 47, 2405–2422, 2008.
640 Tjernström, M., C. Leck, C., Persson, P. O. G., Jensen, M. L., Oncley, S. P., and Targino, A.:
641 The summertime Arctic atmosphere: Meteorological measurements during the Arctic
642 Ocean Experiment 2001, B. Am. Meteorol. Soc., 85, 1305–1321, 2004.
643 Turner, D. D., Clough, S. A., Liljegren, J. C., Clothiaux, E. E., Cady-Pereira, K., and Gaustad,
644 K. L.: Retrieving precipitable water vapor and liquid water path from Atmospheric
645 Radiation Measurement (ARM) program's microwave radiometers, IEEE T. Geosci.
646 Remote, 45, 3680–3690, 2007.
647 Verlinde, J., Harrington, J. Y., McFarquhar, G. M., et al.: The Mixed-Phase Arctic Cloud
648 Experiment (M-PACE), B. Am. Meteorol. Soc., 88, 205–221, doi:10.1175/BAMS-88-2-
649 205, 2007.
650 Walsh, J. E. and Chapman, W. L.: Arctic cloud-radiation temperature associations in
651 observational data and atmospheric reanalyses, J. Climate, 11, 3030–3045, 1998.
652 Webb, E. K.: Profile relationships: The log-linear range, and extension to strong stability.
653 Quart. J. Roy. Meteor. Soc., 96, 67–90, 1970.
654 Wise, M., Baustian, K., Koop, T., Freedman, M., Jensen, E., and Tolbert, M.: Depositional
655 ice nucleation onto crystalline hydrated nacl particles: a new mechanism for ice
656 formation in the troposphere, Atmos. Chem. Phys., 12:1121-1134, doi:10.5194/acp-12-
657 1121-2012, 2012.

Yamaguchi, T. and Feingold, G.: Technical note: Large-eddy simulation of cloudy boundary layer with the Advanced Research WRF model, J. Adv. Model. Earth Syst., 4, M09003, doi:10.1029/2012MS000164, 2012.

661 **Figure Captions**

662 **Figure 1:** Sounding measured at 17:34 UTC 8 April 2008 at Barrow, Alaska (71.338N,
663 156.68W). Left) Water vapor mixing ratio (q_v), temperature (T), and potential temperature
664 (Theta), in units of g kg^{-1}, degrees Kelvin, and degrees Kelvin respectively. Right) Zonal
665 wind (U) and meridional wind (V), in units of m s^{-1}. Gray shading marks the extent of the
666 cloud layer. The dashed lines show the initial profiles used in the WRFLES experiments. The
667 dashed line overlaying water vapor mixing ratio is the initial profile for the total water
668 mixing ratio.

669 **Figure 2:** IN number concentration active at water saturation vs. temperature based on the
670 empirical relationship derived in DeMott et al. (2010) (blue line) used to initialize IN number
671 concentration in each bin. Black vertical lines indicate threshold temperatures for nucleation
672 in the 16 IN bins. Note additional IN become available for nucleation at colder temperatures,
673 such that, for example, at -20.2^{o}C (the coldest temperature in the Control simulation) the total
674 number of IN available for activation is ~1.5 L^{-1}.

675 **Figure 3:** Sensitivity of ice water path to the parameter F in equation (2). Note the similar ice
676 water paths for F=4 and F=6 (total N_{IN} initial values 5.8 and 8.7 L^{-1}, respectively).

677 **Figure 4:** A,B,D) Sensitivity of LWP and IWP to snow density and fall speeds. LWP shown
678 with solid lines and IWP shown with dashed lines, in units of g m^{-2}. C) Fall speeds used in
679 sensitivity studies, in units of m s^{-1}. A) Sensitivity to reducing snow density from 100 kg m^{-3}
680 to 50 kg m^{-3} (red lines) using Control (CNT) fall speeds (red line in C). B) Sensitivity to
681 reducing snow fall speeds (green line in C) using Control snow density (red lines). D)
682 Sensitivity to increasing snow fall speeds (blue line in C) using Control snow density (red

683 lines).

684 **Figure 5:** Simulated ice particle number size distributions using in-cloud mass and number
685 concentrations. Ice water mixing ratio = 3e-4 g/kg, ice number concentration = 0.4/L, snow
686 water mixing ratio = 2.4e-2 g/kg, snow number concentration = 0.45/L.

687 **Figure 6:** (A) N_{IN} and (B) N_{ICE} averaged over 0.5 hours at hour 20, in units of L^{-1} hr^{-1}. Grey
688 shading indicates the extent of the cloud layer. Green dash lines indicate the top and bottom
689 of the mixed layer.

690 **Figure 7:** Time-height cross sections of horizontally-averaged (A) IN advection plus
691 subsidence, in units of $L^{-1}hour^{-1}$, (B) ice plus snow number concentration, in units of L^{-1}, (C)
692 water vapor mixing ratio, in units of g kg^{-1}, and (D) relative humidity with respect to ice, in
693 units of percent, from CNT simulation. Temperature, in units of °C, shown with black
694 contour lines in (B,C,D).

695 **Figure 8:** Control and NoRecycle time series for hours 6-40 (smoothed with 90 minute
696 running average). NoRecycle shown with red and black dashed lines. A) LWP (black) and
697 IWP (red), in units of g m^{-2}. B) Minimum horizontally-averaged temperature in the column,
698 in units of ^{o}C. C) Mixed-layer depth (blue), top height (red), and base height (black), in units
699 of km. D) N_{ICE} integrated over cloud layer (referred to as CL, red) and N_{IN} integrated over
700 subcloud layer (referred to as SubCL, black), in units of m L^{-1}(i.e., meters/liter).

701 **Figure 9:** Horizontally-averaged fluxes from Control and NoRecycle integrations for hours
702 6-40 (smoothed with 90 minute running average). NoRecycle shown with red and black
703 dashed lines. A) N_{ICE} flux at cloud base due to turbulence+subsidence+precipitation (red),

mixed-layer base due to turbulence+subsidence+precipitation (black), and due to activation (multiplied by -1, blue), in units of m L^{-1} hr^{-1}. B) N_{IN} flux at cloud base (indicated by CB in legend) due to turbulence (red), N_{IN} flux due to sublimation (black), and precipitation of N_{ICE} at cloud base (multiplied by -1, blue), in units of m L^{-1} hr^{-1}. C) N_{IN} entrainment at mixed-layer top (red) and base (black), in units of m L^{-1} hr^{-1}.

Figure 10: Schematic of feedback loops that maintain ice production and the phase-partitioning between cloud liquid and ice in an AMPS. Red colors denote N_{IN}. Blue colors denote N_{ICE}. The size of the arrow indicates the relative magnitude of the flux. Vertical profiles of N_{ICE}, N_{IN}, relative humidity, and temperature shown with thin blue, red, green, and yellow lines, respectively.

Figure 11: A) LWP (black) and IWP (red), in units of g m^{-2}. (B) Downward surface shortwave radiation and turbulent kinetic energy (TKE) at cloud base, in units of Wm^{-2} and m^2s^{-2}, respectively. C) N_{ICE} in cloud layer (referred to as CL, red) and N_{IN} in subcloud layer (referred to as SubCL, black), in units of m L^{-1}. (D) Total, turbulent, precipitation N_{ICE} flux at cloud base (referred to as CL base, red, green, blue, respectively) and total N_{ICE} flux at mixed-layer base (referred to as ML base, black), in units of m L^{-1} hr^{-1}, for the SW integration for hours 16-76. Grey shading indicates hours with zero downwelling surface shortwave radiation. E) N_{IN} entrainment at mixed-layer top (red) and base (black), in units of m L^{-1} hr^{-1}. (F) N_{IN} flux at cloud base due to turbulence (red), N_{IN} flux due to sublimation (black), and activation of N_{ICE} (blue), in units of m L^{-1} hr^{-1}.

Figure 12: A) Phase diagram of TKE at cloud base vs. N_{ICE} in the cloud layer starting at peak shortwave hour 40, in units of m L^{-1} and m L^{-1} hr^{-1}, respectively. Colors show sublimation in units of m L^{-1} hr^{-1}. H) 24-hour phase diagrams of sublimation vs. minimum relative humidity in the subcloud layer starting at peak shortwave hour 40, in units of m L^{-1} hr^{-1} and %, respectively. Colors show total N_{ICE} flux at cloud base, m L^{-1} hr^{-1}. Hours 42-47, 47-50, 50-56, and 57-62 indicated with green, blue, black, red arrows, respectively. Minimum shortwave indicated with the moon symbol. Maximum shortwave indicated with the sun symbol.

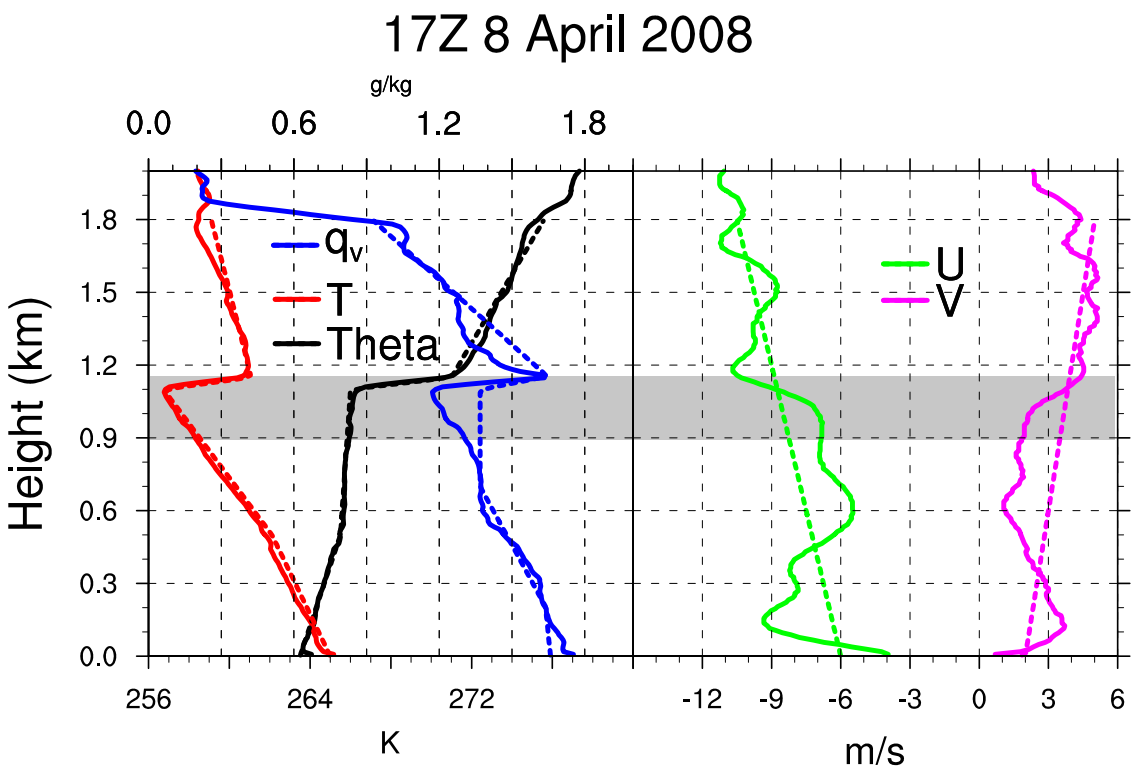

733 **Figure 1:** Sounding measured at 17:34 UTC 8 April 2008 at Barrow, Alaska (71.338N,
734 156.68W). Left) Water vapor mixing ratio (q_v), temperature (T), and potential temperature
735 (Theta), in units of g kg^{-1}, degrees Kelvin, and degrees Kelvin respectively. Right) Zonal
736 wind (U) and meridional wind (V), in units of m s^{-1}. Gray shading marks the extent of the
737 cloud layer. The dashed lines show the initial profiles used in the WRFLES experiments. The
738 dashed line overlaying water vapor mixing ratio is the initial profile for the total water
739 mixing ratio.

740

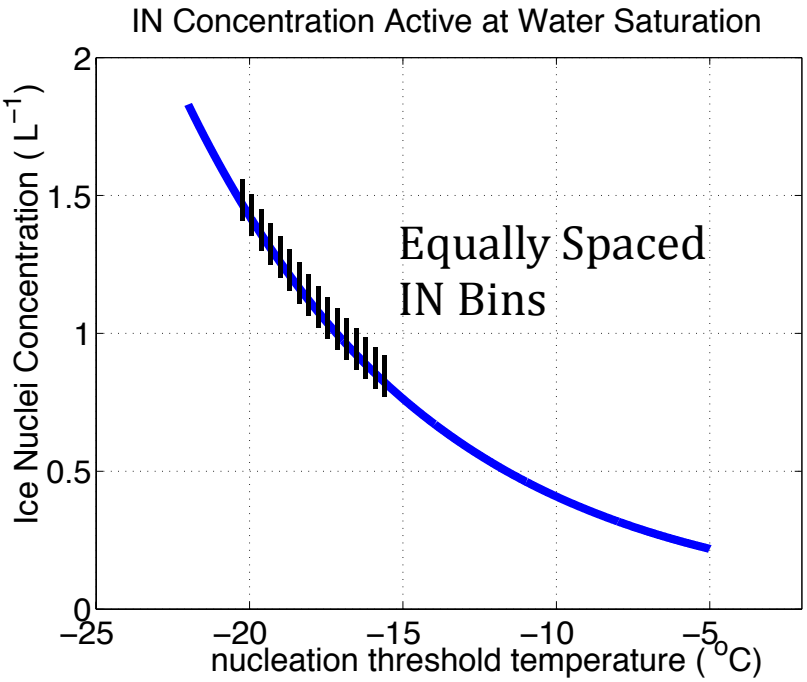

741
742

743 **Figure 2:** IN number concentration active at water saturation vs. temperature based on the
744 empirical relationship derived in DeMott et al. (2010) (blue line) used to initialize IN number
745 concentration in each bin. Black vertical lines indicate threshold temperatures for nucleation
746 in the 16 IN bins. Note additional IN become available for nucleation at colder temperatures,
747 such that, for example, at -20.2^{o}C (the coldest temperature in the Control simulation) the total
748 number of IN available for activation is ~1.5 L^{-1}.

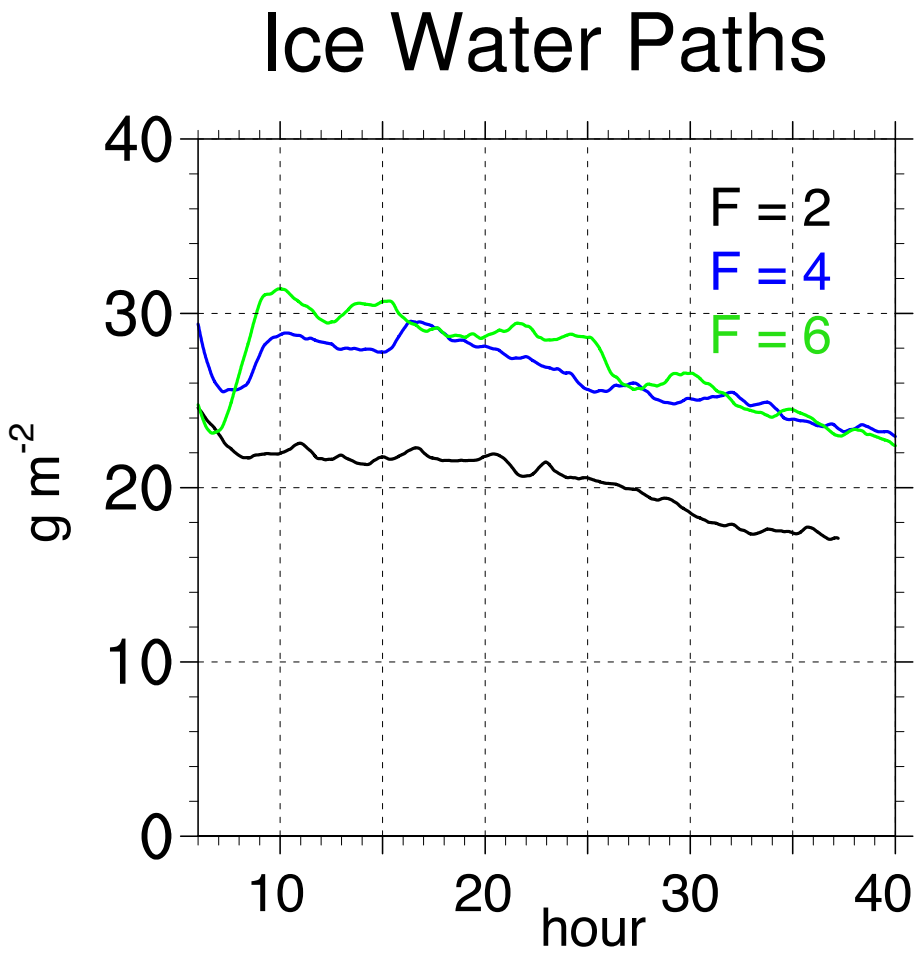

Figure 3: Sensitivity of ice water path to the parameter F in equation (2). Note the similar ice water paths for F=4 and F=6 (total N_{IN} initial values of 5.8 and 8.7 L^{-1}, respectively).

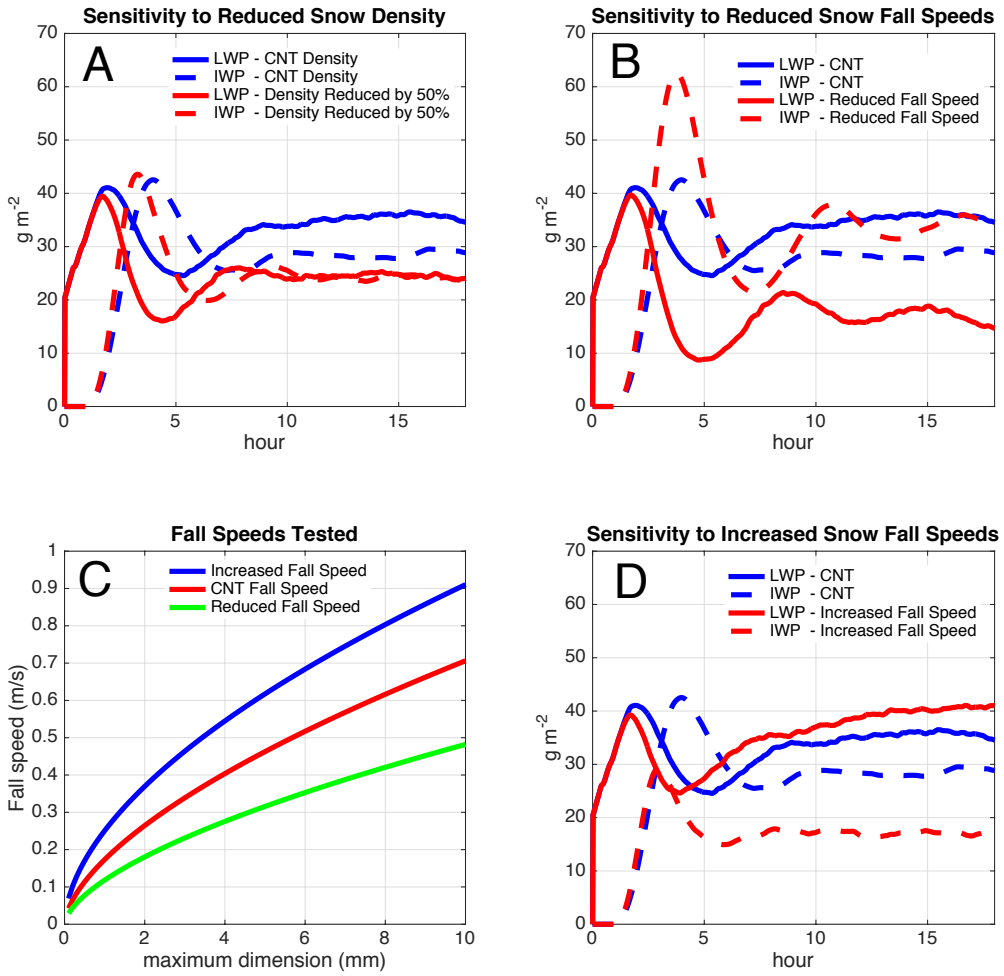

752

753 **Figure 4:** A,B,D) Sensitivity of LWP and IWP to snow density and fall speeds. LWP shown
754 with solid lines and IWP shown with dashed lines, in units of g m^{-2}. C) Fall speeds used in
755 sensitivity studies, in units of m s^{-1}. A) Sensitivity to reducing snow density from 100 kg m^{-3}
756 to 50 kg m^{-3} (red lines) using Control (CNT) fall speeds (red line in C). B) Sensitivity to
757 reducing snow fall speeds (green line in C) using Control snow density (red lines). D)
758 Sensitivity to increasing snow fall speeds (blue line in C) using Control snow density (red
759 lines).

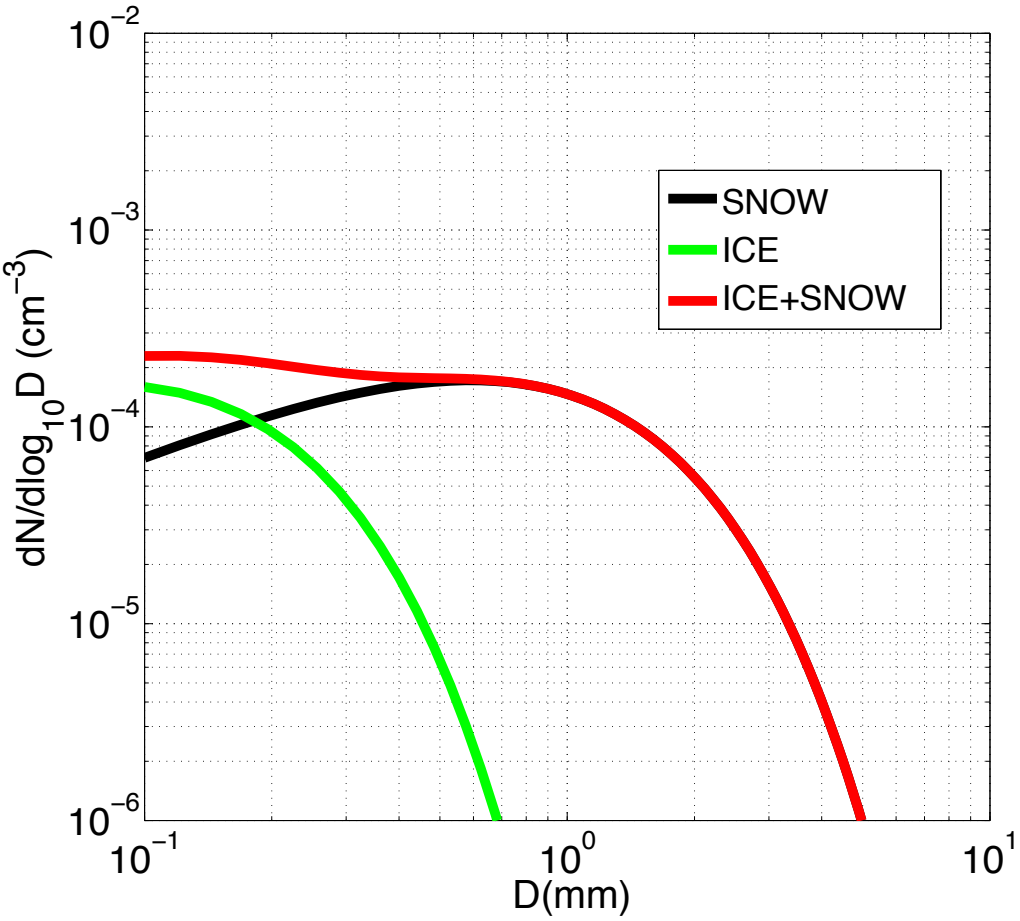

760

761 **Figure 5:** Simulated ice particle number size distributions using in-cloud mass and number

762 concentrations. Ice water mixing ratio = 3e-4 g/kg, ice number concentration = 0.4/L, snow

763 water mixing ratio = 2.4e-2 g/kg, snow number concentration = 0.45/L.

764

765

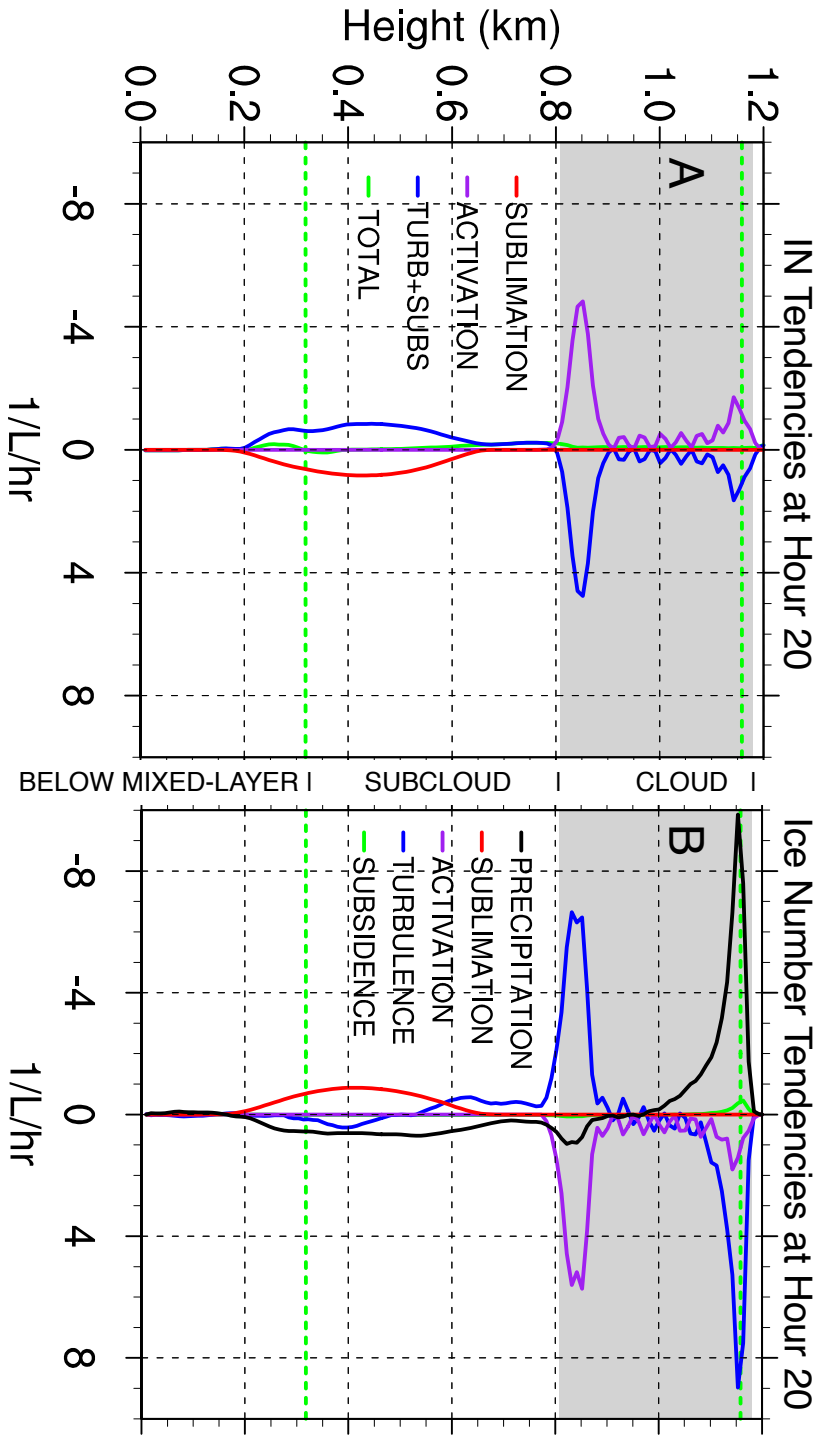

766 **Figure 6:** (A) N_{IN} and (B) N_{ICE} averaged over 0.5 hours at hour 20, in units of L^{-1} hr^{-1}. Grey
767 shading indicates the extent of the cloud layer. Green dash lines indicate the top and bottom
768 of the mixed layer.

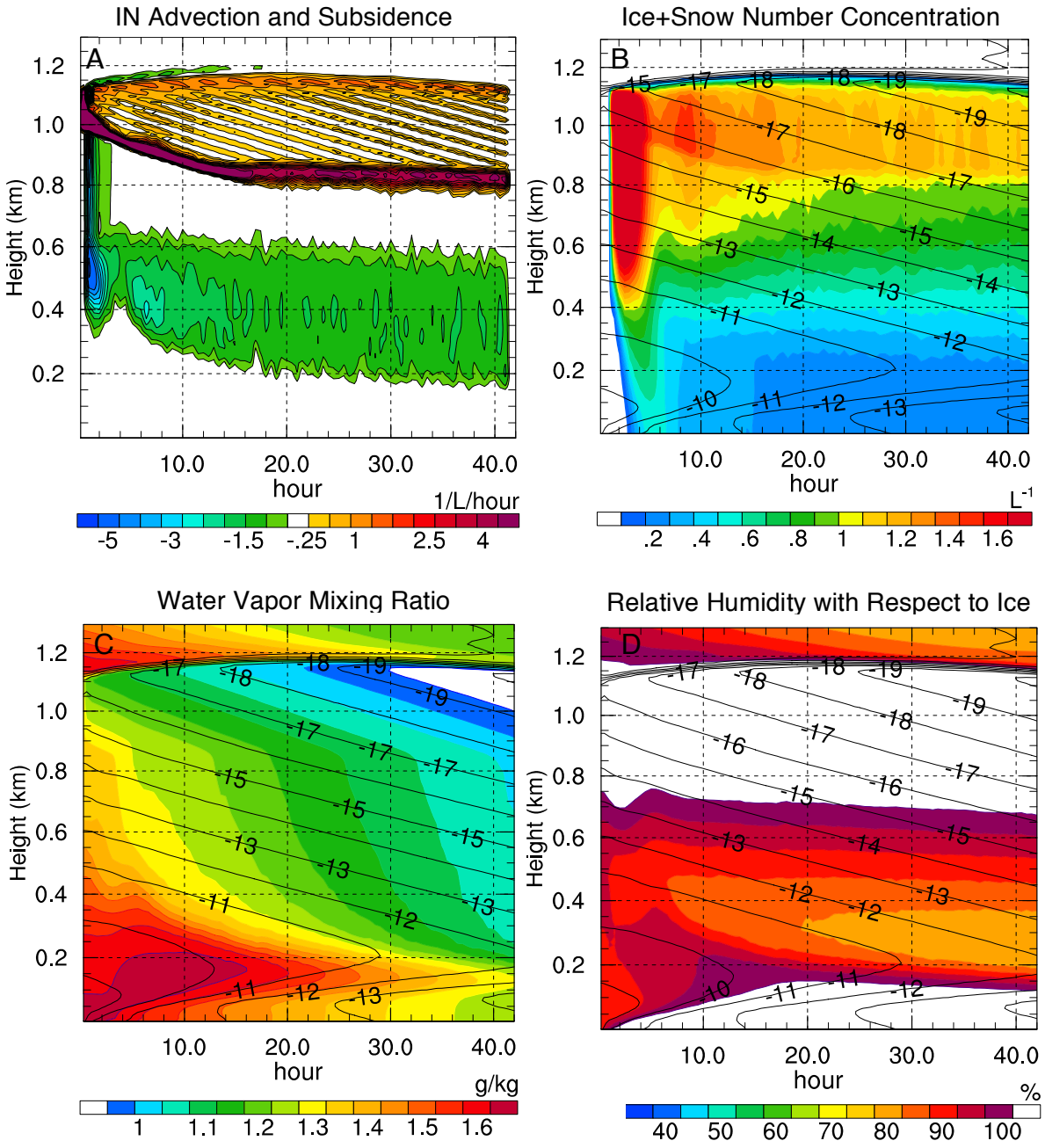

Figure 7: Time-height cross sections of horizontally-averaged (A) IN advection plus subsidence, in units of $L^{-1}hour^{-1}$, (B) ice plus snow number concentration, in units of L^{-1}, (C) water vapor mixing ratio, in units of g kg^{-1}, and (D) relative humidity with respect to ice, in units of percent, from CNT simulation. Temperature, in units of °C, shown with black contour lines in (B,C,D).

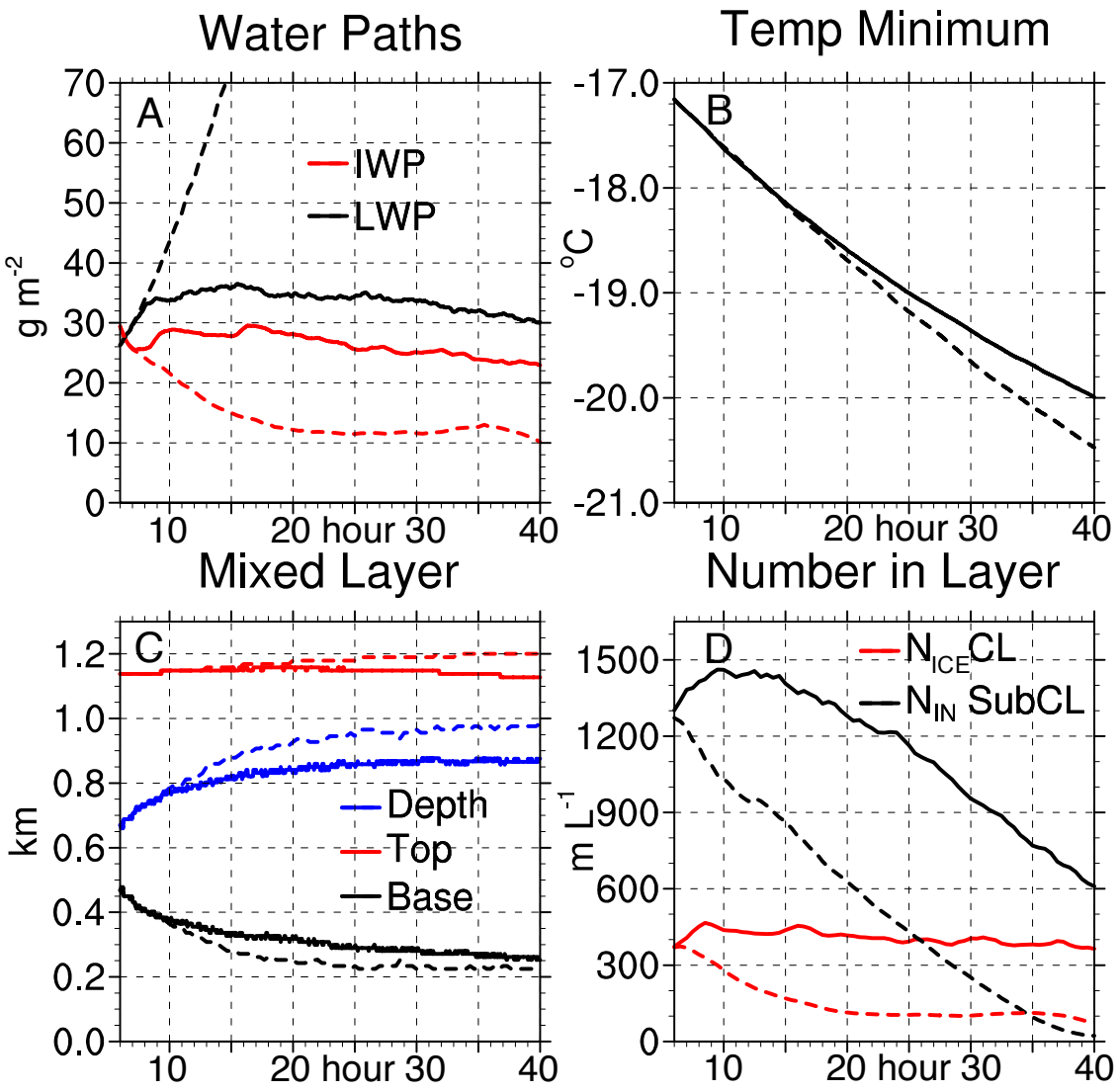

Figure 8: Control and NoRecycle time series for hours 6-40 (smoothed with 90 minute running average). NoRecycle shown with red and black dashed lines. A) LWP (black) and IWP (red), in units of g m^{-2}. B) Minimum horizontally-averaged temperature in the column, in units of ^{o}C. C) Mixed-layer depth (blue), top height (red), and base height (black), in units of km. D) N_{ICE} integrated over cloud layer (referred to as CL, red) and N_{IN} integrated over subcloud layer (referred to as SubCL, black), in units of m L^{-1}(i.e., meters/liter).

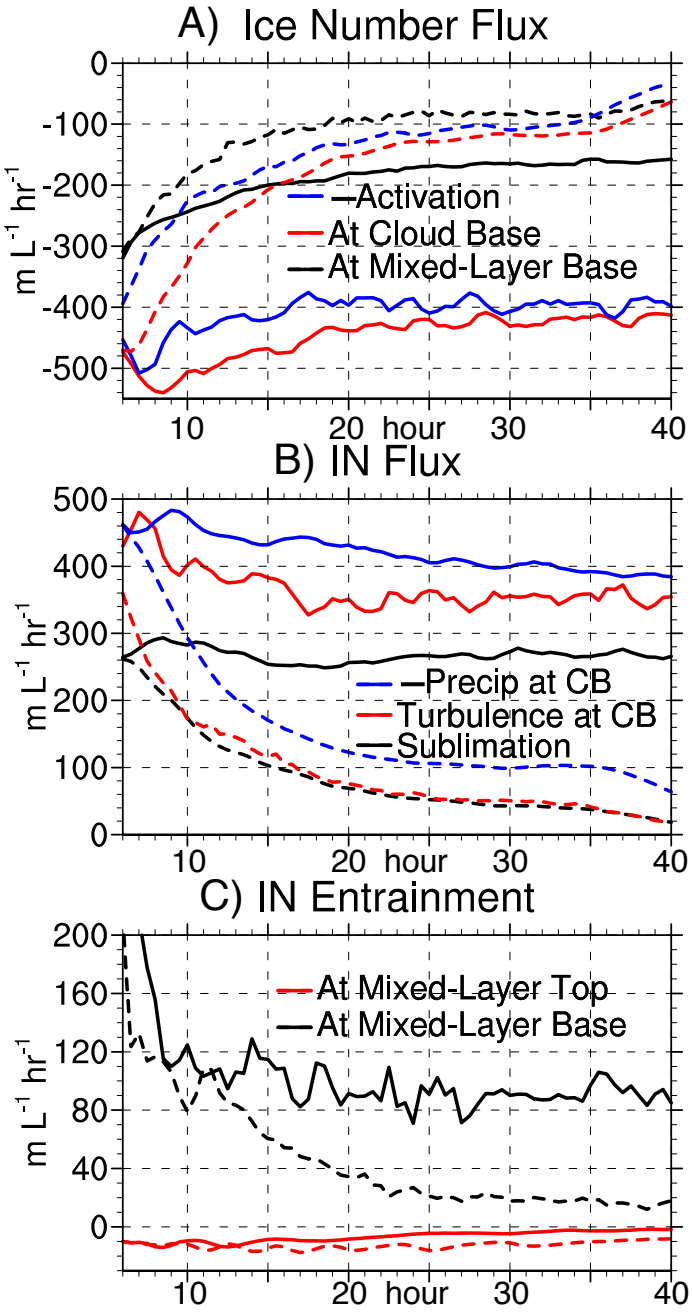

784

785 **Figure 9:** Horizontally-averaged fluxes from Control and NoRecycle integrations for hours
786 6-40 (smoothed with 90 minute running average). NoRecycle shown with dashed lines. A)
787 N_{ICE} flux at cloud base due to turbulence+subsidence+precipitation (red), mixed-layer base
788 due to turbulence+subsidence+precipitation (black), and due to activation (multiplied by -1,
789 blue), in units of m L^{-1} hr^{-1}. B) N_{IN} flux at cloud base (indicated by CB in legend) due to
790 turbulence (red), N_{IN} flux due to sublimation (black), and precipitation of N_{ICE} at cloud base
791 (multiplied by -1, blue), in units of m L^{-1} hr^{-1}. C) N_{IN} entrainment at mixed-layer top (red)
792 and base (black), in units of m L^{-1} hr^{-1}.

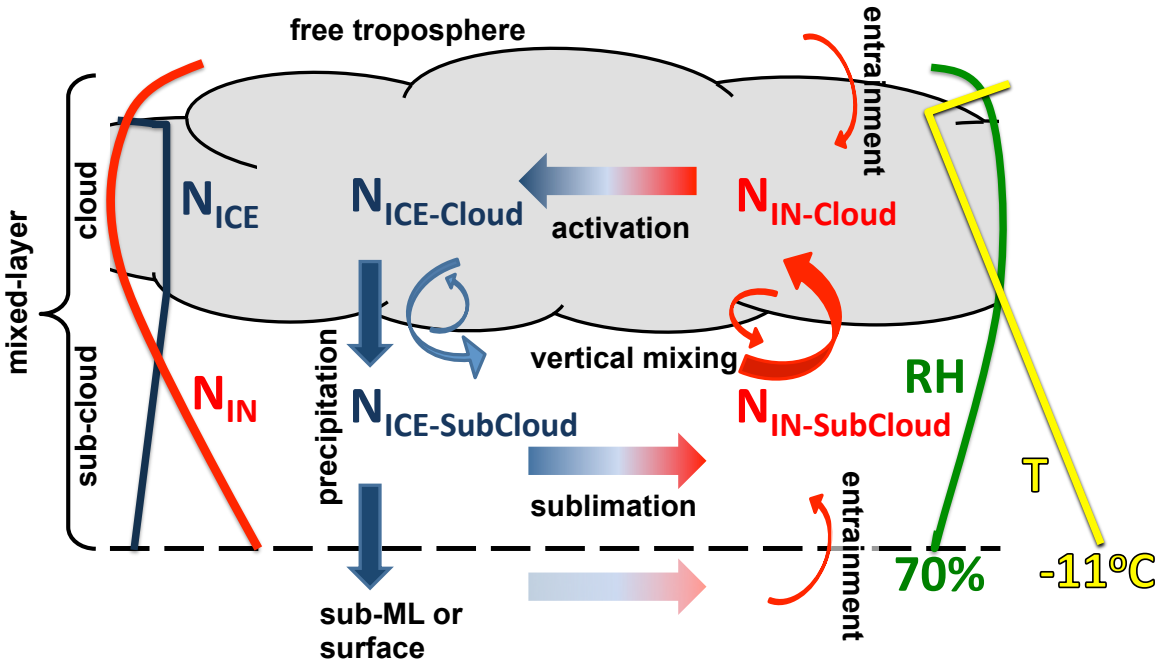

793

794 **Figure 10:** Schematic of feedback loops that maintain ice production and the phase-
795 partitioning between cloud liquid and ice in AMPS when recycling is allowed. Red colors
796 denote N_{IN}. Blue colors denote N_{ICE}. Vertical profiles of N_{ICE}, N_{IN}, relative humidity, and
797 temperature shown with thin blue, red, green, and yellow lines, respectively.

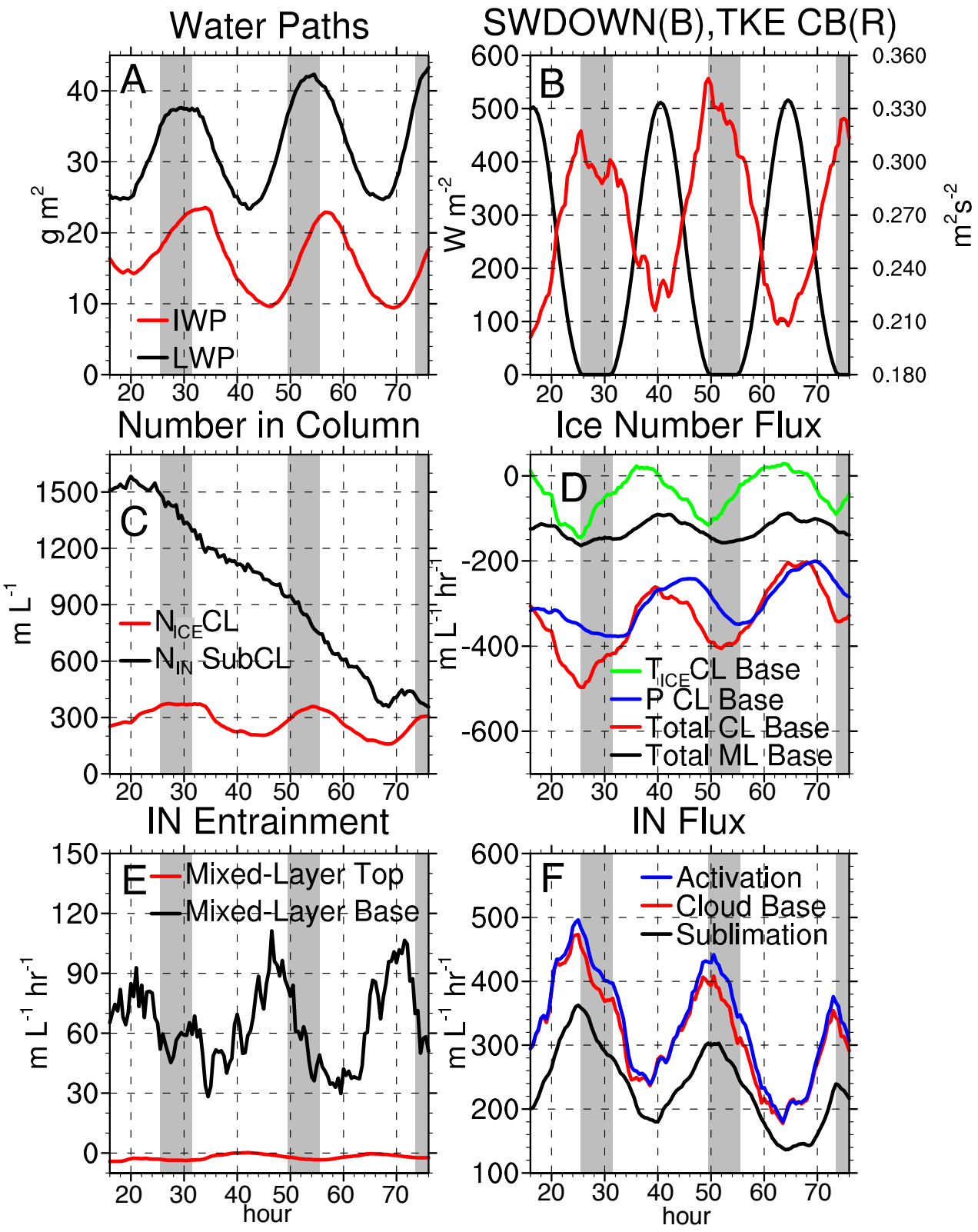

798

799 **Figure 11:** SW time series (see Figure captions).

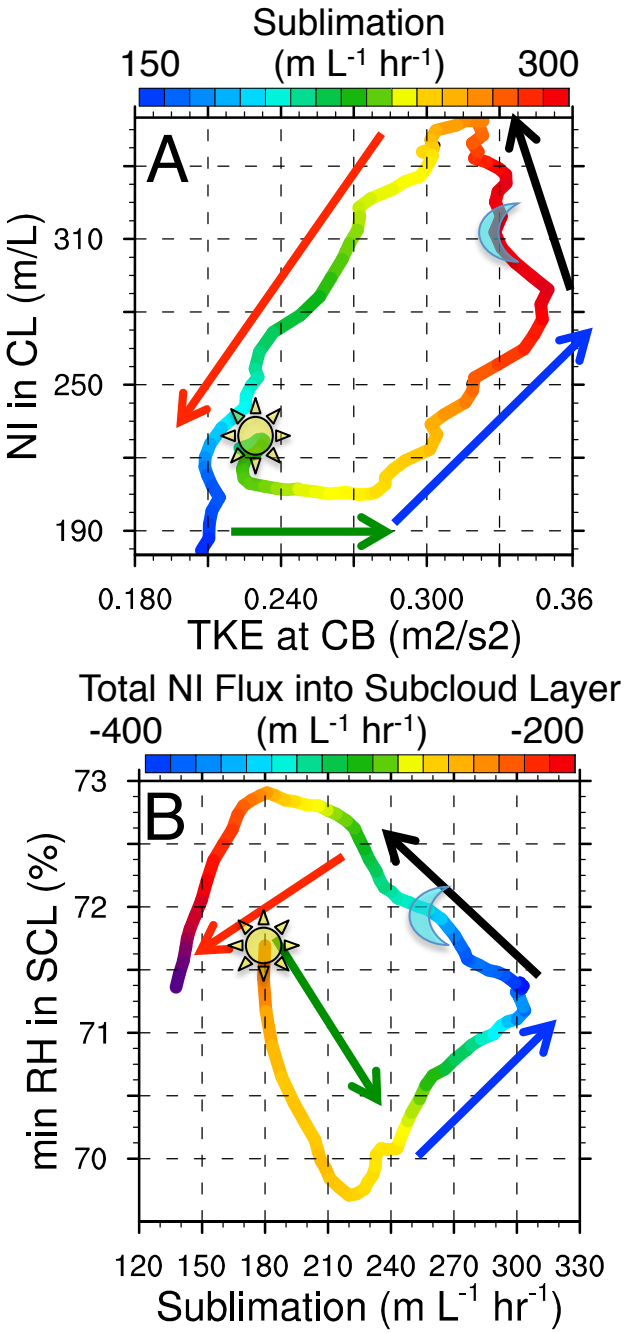

800

801 **Figure 12:** A) Phase diagram of TKE at cloud base vs. N_{ICE} in the cloud layer starting at
802 peak shortwave hour 40, in units of m L^{-1} and m L^{-1} hr^{-1}, respectively. Colors show
803 sublimation in units of m L^{-1} hr^{-1}. B) 24-hour phase diagrams of sublimation vs. minimum
804 relative humidity in the subcloud layer starting at peak shortwave hour 40, in units of m L^{-1}
805 hr^{-1} and %, respectively. Colors show total N_{ICE} flux at cloud base, m L^{-1} hr^{-1}. Hours 42-47,
806 47-50, 50-56, and 57-62 indicated with green, blue, black, red arrows, respectively.

807 Minimum shortwave indicated with the moon symbol. Maximum shortwave indicated with
808 the sun symbol.